AVOID CATASTROPHIC FORGETTING WITH RANK-1 FISHER FROM DIFFUSION MODELS

Anonymous authors
Paper under double-blind review

ABSTRACT

Catastrophic forgetting remains a central obstacle for continual learning in neural models. Popular approaches—replay and elastic weight consolidation (EWC)—have limitations: replay requires a strong generator and is prone to distributional drift, while EWC implicitly assumes a shared optimum across tasks and typically uses a diagonal Fisher approximation. In this work, we study the gradient geometry of diffusion models, which can already produce high-quality replay data. We provide theoretical and empirical evidence that, in the low signal-to-noise ratio (SNR) regime, per-sample gradients become strongly collinear, yielding an empirical Fisher that is effectively rank-1 and aligned with the mean gradient. Leveraging this structure, we propose a rank-1 variant of EWC that is as cheap as the diagonal approximation yet captures the dominant curvature direction. We pair this penalty with a replay-based approach to encourage parameter sharing across tasks while mitigating drift. On class-incremental image generation datasets (MNIST, FashionMNIST, CIFAR-10, ImageNet-1k), our method consistently improves average FID and reduces forgetting relative to replay-only and diagonal-EWC baselines. In particular, forgetting is nearly eliminated on MNIST and FashionMNIST and is roughly halved on ImageNet-1k. These results suggest that diffusion models admit an approximately rank-1 Fisher. With a better Fisher estimate, EWC becomes a strong complement to replay: replay encourages parameter sharing across tasks, while EWC effectively constrains replay-induced drift.

1 INTRODUCTION

The task of continual learning aims to train neural models on a stream of tasks without revisiting the full past data. A long–standing obstacle is catastrophic forgetting—when learning new tasks drastically degrades performance on earlier ones (McCloskey & Cohen, 1989; French, 1999; Parisi et al., 2019). In contrast, humans exhibit a striking robustness to interference, partly due to systems-level mechanisms such as memory consolidation and replay in the hippocampal–neocortical loop (McClelland et al., 1995; McGaugh, 2000; Foster & Wilson, 2006). These observations have inspired a family of continual learning methods that explicitly encode consolidation or replay in training deep networks on continuous tasks.

Two representative approaches are elastic weight consolidation (EWC) (Kirkpatrick et al., 2017) and generative replay (Shin et al., 2017). EWC constrains parameter changes with a quadratic penalty weighted by an estimate of the Fisher information at a previously learned task, constraining updates to remain near parameter directions that support old tasks (Kirkpatrick et al., 2017; Schwarz et al., 2018). Intuitively, EWC behaves like an online consolidation process that selectively "stiffens" important parameters. Generative replay maintains a generator and distills samples from past tasks while learning new ones, thereby approximating rehearsal without storing original data (Shin et al., 2017; van de Ven & Tolias, 2018). However, replay inherits the generator's imperfections and can amplify distributional shift. EWC in practice relies on a diagonal Fisher approximation, which neglects cross-parameter correlations and struggles to find a shared parameter space between tasks in overparameterized models, particularly when tasks have disjoint optimum. These observations suggest a complementary pairing: replay can encourage parameter sharing by exposing shared data support, while a stronger approximation to Fisher information can constrain updates and mitigate replay's residual shift.

In this work, we study the gradient behavior of diffusion models (Ho et al., 2020b; Nichol & Dhariwal, 2021), which are already capable of generating high quality replay data. Our starting point is the observation that diffusion models admit a tractable gradient structure when the signal-to-noise ratio (SNR) is lower (at later timesteps). As a model converges, the per-sample gradients g become approximately collinear with their mean u. This makes the empirical Fisher F effectively rank-1:

$$F \;=\; \mathbb{E}\big[g\,g^{\top}\big] \;\approx\; \alpha\,u\,u^{\top}, \quad u = \mathbb{E}[g],$$

This yields a consolidation penalty that captures the dominant curvature direction "for free" from model gradients. In contrast, the commonly used diagonal Fisher approximation captures almost no curvature when SNR is low. We leverage this structure to instantiate a rank-1 EWC that complements generative replay: replay encourages cross-task parameter overlap while our proposed rank-1 EWC constrains updates along the principal sensitive direction to the shared optimum across tasks.

Our main contributions are: (1) We provide both theoretical and empirical characterizations of Fisher information geometry in diffusion models, showing that low SNR induces a near rank-1 Fisher aligned with the mean gradient. (2) We propose a practical rank-1 EWC penalty that is as cheap as a diagonal penalty but captures more curvature information for diffusion models. (3) We demonstrate that combining rank-1 EWC with distillation-based replay substantially reduces forgetting in continual image generation tasks, improving generation fidelity and stability across long horizons. On MNIST, FashionMNIST, CIFAR-10, and ImageNet-1k, our method consistently outperforms replay-only and diagonal Fisher baselines. In particular, forgetting is nearly eliminated on MNIST and FashionMNIST and is roughly halved on ImageNet-1k, the longest-horizon setting, relative to baselines.

2 Background and related work

2.1 Diffusion models

Diffusion models are a family of generative models that define a fixed forward noising process and learn a reverse (denoising) process that maps Gaussian noise to data (Sohl-Dickstein et al., 2015; Ho et al., 2020a). The forward chain corrupts data $x_0 \sim q_0$ via a Markov process

$$q(x_t \mid x_{t-1}) \;\sim\; \mathcal{N}\big(\sqrt{1-\beta_t}\,x_{t-1},\, \beta_t\mathbf{I}\big), \quad q(x_t \mid x_0) \;\sim\; \mathcal{N}\big(\sqrt{\bar{\alpha}_t}\,x_0,\, (1-\bar{\alpha}_t)\mathbf{I}\big),$$

where $\alpha_t = 1-\beta_t$, $\bar{\alpha}_t = \prod_{s=1}^{t}\alpha_s$, $\beta_t \in (0,1)$ is the noise level, and $t \in \{0 \cdots N\}$ is the discrete forward noising process timestep. The reverse transitions $p_\theta(x_{t-1}\,|\,x_t)$ are parameterized by a neural network ε_θ and trained by maximizing a variational lower bound (ELBO). In practice, the ELBO reduces to a reweighted denoising loss (Ho et al., 2020a):

$$\mathcal{L}_{\text{simple}}(\theta) \;=\; \frac{1}{2}\mathbb{E}_{t,\,x_0,\,\varepsilon\sim\mathcal{N}(0,\mathbf{I})}\Big[\;\big\|\varepsilon - \varepsilon_\theta(x_t,t)\big\|_2^2\;\Big], \quad x_t = \sqrt{\bar{\alpha}_t}x_0 + \sqrt{1-\bar{\alpha}_t}\,\varepsilon.$$

This surrogate loss can be interpreted as a score-based generative modeling that estimates the score $\nabla_{x_t}\log q_t(x_t)$ at each timestep, where $q_t(x_t) = \int q(x_t \mid x_0)q_0(x_0)dx_0$, and then integrates a reverse-time SDE/ODE to sample (Song & Ermon, 2019; Song et al., 2021b; Vincent, 2011; Hyvärinen, 2005): $\nabla_{x_t}\log q_t(x_t) = -\frac{1}{\sqrt{1-\bar{\alpha}_t}}\,\mathbb{E}[\varepsilon \mid x_t]$, and the model's score estimate follows from $s_\theta(x_t,t) \;=\; -\frac{1}{\sqrt{1-\bar{\alpha}_t}}\,\varepsilon_\theta(x_t,t)$, where $\varepsilon_\theta(x_t,t) = \mathbb{E}[\varepsilon \mid x_t]$ at model optimum.

Denoising Diffusion Implicit Models (Song et al., 2021a) further show that one can define a non-Markovian, deterministic sampling path that preserves DDPM's per-time marginal distributions while allowing far fewer steps. In this work, we use a DDIM sampling process for faster image generation.

2.2 Elastic weight consolidation

Elastic weight consolidation mitigates catastrophic forgetting by regularizing parameter updates using information about how important each weight was to previously learned tasks (Kirkpatrick et al., 2017). It casts continual learning as approximate Bayesian updating: for tasks 1:T, the posterior factors as $p(\theta \mid \mathcal{D}_{1:T}) \propto p(\mathcal{D}_T \mid \theta)\,p(\theta \mid \mathcal{D}_{1:T-1})$. EWC approximates the previous-task posterior $p(\theta \mid \mathcal{D}_{1:T-1})$ with a Laplace approximation around the prior optimum $\theta^{\star}_{T-1}$, yielding $-\log p(\theta \mid \mathcal{D}_{1:T-1}) \;\approx\; \frac{1}{2}\,(\theta-\theta^{\star}_{T-1})^{\top}F^{(T-1)}(\theta-\theta^{\star}_{T-1})$, where $F^{(T-1)}$ is the Fisher information evaluated at $\theta^\star_{T-1}$. Plugging this quadratic surrogate into the negative log-posterior for task k gives the EWC objective

$$\mathcal{L}_{\text{EWC}}(\theta) \;=\; \mathcal{L}_T(\theta) \;+\; \frac{\lambda}{2}\sum_{k=1}^{T-1}(\theta-\theta^\star_k)^\top F^{(k)}(\theta-\theta^\star_k), \tag{1}$$

with λ trading off plasticity and stability. Intuitively, parameters with high curvature under the previous task are penalized more strongly, discouraging changes that would degrade old performance. In the original work, $\mathcal{L}_T(\theta)$ is the negative log-likelihood for a classification model. For latent-variable generative models such as diffusion models, one can replace this term with a tractable variational surrogate such as the negative ELBO.

In practice, a diagonal Fisher is often used as an approximation to the full Fisher. In this work, we show that diffusion models approximate a rank-1 Fisher for free for a more effective application in continual learning.

2.3 Continual learning with generative models

Continual learning trains a model on a sequence of tasks, posing the dual challenge of adapting to distribution shift while preserving knowledge from earlier tasks. Broadly, continual learning approaches fall into (i) regularization-based constraints on parameter drift (e.g., EWC) and (ii) replay-based strategies that rehearse past knowledge (Kirkpatrick et al., 2017; van de Ven & Tolias, 2018). For generative models, especially diffusion models, replay is particularly natural because the model can synthesize high-fidelity samples for rehearsal (Ho et al., 2020a).

DDGR uses a diffusion generator with class conditioning to synthesize exemplars of prior tasks, and diffusion-based replay has been adapted to dense prediction (segmentation, detection) using task-specific guidance or pseudo-labels (Gao et al., 2023; Chen et al., 2023; Kim et al., 2024). However, naïve replay with continually updated diffusion models can degrade denoising because the reverse process itself drifts across tasks. Recent work on generative distillation mitigates this by distilling the entire reverse chain ($\theta^*_{t-1} \to \theta_t$) across timesteps, aligning noise predictions so the continually trained model retains both sample quality and coverage of past tasks (Masip et al., 2025). In this work, we employ generative distillation along with our approach to EWC for a more effective learning.

3 Diffusion models approximate the rank-1 Fisher

The Bayesian view of the continual learning suggests that $p(\theta \mid \mathcal{D}_{1:T}) \propto p(\mathcal{D}_T \mid \theta)\, p(\theta \mid \mathcal{D}_{1:T-1})$ where $\mathcal{D}_T$ is the dataset for task T and θ represents the model parameters. EWC (Kirkpatrick et al., 2017) proposed a Laplace approximation of the posterior distribution $p(\theta \mid \mathcal{D}_{1:T-1})$ for previous tasks as $-\log p(\theta \mid \mathcal{D}_{1:T-1}) \;\approx\; \frac{1}{2}(\theta-\theta^\star_{T-1})^\top F^{(T-1)}(\theta-\theta^\star_{T-1})$, where $F^{(T-1)}$ is the Fisher information matrix for the previous task. However, forming a full Fisher is impractical and a diagonal approximation is widely used. In this work, we show that the Fisher of a diffusion model can be approximated as a rank-1 structure, which better captures important weights associated with previous tasks. We theoretically analyze why diffusion models approximate a rank-1 Fisher in Section 3.1 along with empirical analysis in Section 3.2. We then derive the practical EWC loss using rank-1 Fisher in Section 3.3 and complement it with generative distillation in Section 3.4.

3.1 Per-sample gradients align with their mean

Setup and notations. We use the standard variance-preserving forward process

$$x_t \;=\; \sqrt{\bar\alpha_t}\,x_0 \;+\; \sqrt{1-\bar\alpha_t}\,\varepsilon, \quad \varepsilon \sim \mathcal{N}(0,I), \quad t \in \{1\cdots N\}$$

If we let $\varepsilon_\theta(x_t,t)$ be the noise prediction network, the per-sample surrogate loss (Ho et al., 2020a) is:

$$\mathcal{L}_{\text{simple}}(\theta;x_t) \;=\; \tfrac{1}{2}\left\|\varepsilon-\varepsilon_\theta(x_t,t)\right\|_2^2. \tag{2}$$

From a denoise score-matching perspective, let model score $s_\theta(x_t,t) := \nabla_{x_t}\log p_\theta(x_t)$ and the true marginal score $s^\star_t(x_t) := \nabla_{x_t}\log q_t(x_t)$, where q_t denotes the noisy data distribution at time t

and let p_θ be the model with parameters θ. The connection to per-sample $\mathcal{L}_{\text{simple}}$ can expressed as follows (Ho et al., 2020a; Vincent, 2011; Song et al., 2021b):

$$\varepsilon_\theta(x_t, t) \;=\; -\sqrt{1-\bar{\alpha}_t}\; s_\theta(x_t, t), \quad \mathbb{E}\left[\varepsilon \mid x_t\right] \;=\; -\sqrt{1-\bar{\alpha}_t}\; s_t^\star(x_t) \tag{3}$$

Substituting Equation 3 into Equation 2 yields the per-sample denoising score-matching loss:

$$\mathcal{L}_{DSM}(\theta; x_t) \;=\; \frac{1-\bar{\alpha}_t}{2}\left\| s_\theta(x_t, t) - s_t^\star(x_t)\right\|_2^2, \tag{4}$$

Additionally, we define $\sqrt{\bar{\alpha}_t}$ as the signal level and $1-\bar{\alpha}_t$ as the noise level at time t. The signal-to-noise ratio *SNR* $:= \sqrt{\bar{\alpha}_t}/(1-\bar{\alpha}_t)$ decreases with t. Intuitively, noise will dominate the signal in the later diffusion timesteps.

Proposition 1. *Let $s_t^\star(x_t)$, $x_t \sim q_t$, be the score of the noisy data distribution at time t in a variance-preserving diffusion process. As SNR decreases, $s_t^\star(x_t) \approx -x_t/(1-\bar{\alpha}_t)$.*

We refer Appendix B.1 for the proof. Proposition 1 shows that in the low SNR region (i.e, at later diffusion timesteps), the score function is approximately predicting its scaled input. In other words, the score function behaves like a scaled identity map from x_t to $-x_t/(1-\bar{\alpha}_t)$ when the SNR is low.

Assumption 1. $s_\theta(x_t, t)$ approximates a linear function $s_\theta(x_t, t) \approx x_t\theta$ when the model learns to perform scaled identity mapping such that $s_\theta(x_t, t) = x_t\gamma_t I \approx x_t\theta,\ \gamma_t \in \mathbb{R}$.

Proposition 2. *As the SNR decreases and the model converges, for any $x_t \sim q_t$, the per-sample gradient $\nabla_\theta \mathcal{L}_{\text{DSM}}(\theta; x_t)$ becomes collinear with its population mean under Assumption 1:*

$$\nabla_\theta \mathcal{L}_{\text{DSM}}(\theta; x_t) \;\propto\; \mathbb{E}_{x_t' \sim q_t}\!\left[\nabla_\theta \mathcal{L}_{\text{DSM}}(\theta; x_t')\right].$$

Proposition 1 suggests that when the SNR is low, $s_t^\star(x_t) \approx x_t\gamma_t$, where $\gamma_t = -1/(1-\bar{\alpha}_t)$, which is a scalar independent of input x_t. Near convergence, $s_\theta(x_t, t) \approx s_t^\star(x_t) \approx x_t\gamma_t$. Assumption 1 hypothesizes that $s_\theta(x_t, t)$ could be linear and takes the form of $s_\theta(x_t, t) = x_t\theta$. This is plausible in practice because a trivial solution for UNet (Ronneberger et al., 2015) is to directly route the inputs to the output due to the skip connections. At a given t such that the SNR is low, $s_\theta(x_t, t) \approx x_t\theta \approx x_t\gamma_t I$. As a result, the gradient of $s_\theta(x_t, t)$ can be understood as the direction that moves θ to $\gamma_t I$. Since $s_\theta(x_t, t) \approx \theta x_t$ is linear, the directional change in θ at each x_t is collinear to $\theta - \gamma_t I$ independent of x_t, so the per-sample gradients are collinear with each other, and hence collinear to their mean. We leave the complete proof in Appendix B.2.

Theorem 1. *Under Proposition 1 and Proposition 2, the empirical Fisher information matrix at time t: $F_t(\theta) = \mathbb{E}_{x_t' \sim q_t}\big[\, g(x_t'; \theta)\, g(x_t'; \theta)^\top \big]$, $g(x_t; \theta) = \nabla_\theta \mathcal{L}_{DSM}(\theta; x_t)$, is approximately rank-1 when the SNR is low with eigenvector $\mu_t(\theta) = \mathbb{E}_{x_t' \sim q_t}[g(x_t'; \theta)]$, and eigenvalue $\frac{\mu_t(\theta)^\top F_t(\theta)\, \mu_t(\theta)}{\|\mu_t(\theta)\|_2^4}$.*

Proof. Let $v_t(\theta) = \mathbb{E}_{x_t' \sim q_t}[g(x_t'; \theta)]$ be the mean of the gradients. By Proposition 2, $g(x_t; \theta) \approx c(x_t) v_t(\theta)$ for some scalar function $c(\cdot)$. Then

$$F_t(\theta) = \mathbb{E}_{x_t' \sim q_t}\left[\, g(x_t'; \theta)\, g(x_t'; \theta)^\top \right] \approx \mathbb{E}_{x_t' \sim q_t}[c^2(x_t')] v_t(\theta) v_t(\theta)^\top \tag{5}$$

Therefore, $F_t(\theta)$ is approximately rank-1 with eigenvector $v_t(\theta) = \mu_t(\theta)$ and eigenvalue $\mathbb{E}_{x_t' \sim q_t}[c^2(x_t')]$. Multiplying 5 by $\mu^\top$ on the left and μ on the right, we get

$$\mu_t^\top(\theta) F_t(\theta) \mu_t(\theta) \approx \mathbb{E}_{x_t' \sim q_t}[c^2(x_t')] \|\mu_t(\theta)\|^4 \implies \mathbb{E}_{x_t' \sim q_t}[c^2(x_t')] \approx \frac{\mu_t(\theta)^\top F_t(\theta)\, \mu_t(\theta)}{\|\mu_t(\theta)\|^4}$$

□

3.2 Empirical validation

Theorem 1 suggests that, under model convergence, diffusion models approximate a rank-1 Fisher information matrix for their gradients as the SNR decreases (i.e., as the forward process timestep increases). To empirically verify this result, we train a small diffusion model on MNIST (Lecun et al., 1998), whose full Fisher matrix fits in GPU memory, and analyze its gradient behavior across timesteps $t = 100, 200, \ldots, 900$. For each t, we sample 1024 data points and compute their gradients. Experiment and model details can be found in Appendix C.

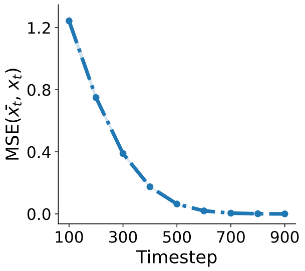

Figure 1: MSE between model input x_t and the scaled prediction $\hat{x_t}$ at each timestep.

We first empirically validate Proposition 1, which states that when SNR is low, the denoising network behaves as a scaled identity map. Let $\varepsilon_\theta(x_t; t) = \hat{\varepsilon}$ be the denoising network, and by Tweedie's identity (Efron, 2011), $\hat{x_t} = \sqrt{1 - \bar{\alpha_t}}\hat{\varepsilon}$. Figure 1 plots the mean-square error between input x_t and prediction $\hat{x_t}$. As timestep increases (SNR decreases), the model begins to perfectly predict its scaled input with error approaching 0.

We then empirically validate Proposition 2 that the per-sample gradients $g(\theta; x_t)$ are collinear with their mean $\mu_t(\theta) = \mathbb{E}_{x'_t \sim q_t}[g(\theta; x'_t)]$ at low SNR when the model converges. For each gradient, we compute the absolute cosine similarity to the population mean. Figure 2 shows these similarities at selected timesteps where each pixel represents a per-sample similarity. We find that per-sample gradients are mostly collinear with their mean at each timestep, with stronger collinearity in the mid-to-late timesteps (i.e. deeper red). This also provides empirical support for Assumption 1 that $s_\theta(x_t, t) \approx x_t\theta$ such that the per-sample gradient becomes a scaled directional change in $\Delta\theta = \theta - \gamma_t I$ that is not dependent on x_t. We additionally plot the pairwise cosine similarities of $\mu_t(\theta)$ across timesteps in Figure 3a. We find that the $\mu_t(\theta)$ for different timesteps highly align with each other. This suggests a practical benefit where we can Monte-Carlo sample timesteps instead of constructing a separate Fisher $F_t(\theta)$ at each timestep.

To probe the rank of the Fisher, we perform eigen decomposition on the empirical Fisher $F_t(\theta)$ from the gradients of the 1024 samples and collect top 5 eigenvalues $\lambda_1 \geq \cdots \geq \lambda_5$. If $F_t(\theta)$ is nearly rank-1, then $\lambda_1 \gg \lambda_2$. In Figure 3b, we plot the top 5 eigenvalues at each timestep in log-scale. We observe that λ_1 is typically one or two orders of magnitude larger than the remaining eigenvalues and their overall magnitude decreases as timestep increases. To quantify the dominance of the leading eigenvalue, we compute the ratio $r_t = \lambda_2/\lambda_1$. Smaller r_t indicates a larger eigengap and stronger rank-1 behavior. Figure 3c indicates that $\lambda_1 \gg \lambda_2$ at all timesteps with the lowest ratio ($r_t = 0.022$) achieved at $t = 700$, suggesting a sharper single-eigenvalue dominance in the low SNR timesteps.

Since Fisher is empirically near rank-1, we compare two approximations at each timestep: (i) the rank-1 reconstruction from Equation 5, and (ii) the diagonal $F_t^{\text{diag}}(\theta)$. For each, we report the relative

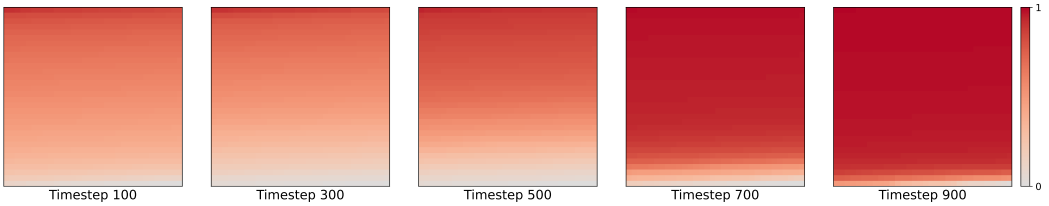

Figure 2: Absolute cosine similarities between per-sample gradient $g(\theta; x_t)$ and their expectation $\mu(\theta)$ at different diffusion timesteps. Each pixel represents a per-sample similarity. Higher values (deeper red) indicate stronger collinearity with $\mu(\theta)$.

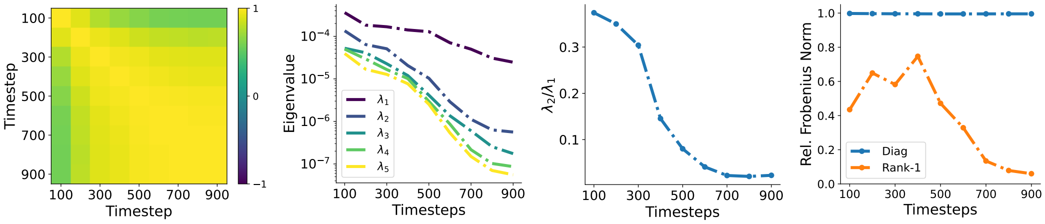

(a) (b) (c) (d)

Figure 3: (a): Pairwise cosine similarities of $\mu_t(\theta)$ across each forward process timestep. (b): Top 5 eigenvalues of $F_t(\theta)$ across timesteps in log-scale. (c): The ratio $r_t = \lambda_2/\lambda_1$ across timesteps. (d): Relative Frobenius norm between $F_t(\theta)$ and diagonal and rank-1 approximations across timesteps.

Frobenius error with respect to the full Fisher: $\mathrm{err}(\widehat{F}_t) = \frac{\|F_t(\theta) - \widehat{F}_t(\theta)\|_F}{\|F_t(\theta)\|_F}$, $\widehat{F}_t \in \{F_t^{\text{rank1}}, F_t^{\text{diag}}\}$, where $\|\cdot\|_F$ is the Frobenius norm. Figure 3d shows that rank-1 approximation achieves a lower error at the mid-to-late timesteps, suggesting that the rank-1 reconstruction is close to the true Fisher. This result aligns with the above two empirical results that the rank-1 structure is clearer in the low SNR timesteps. It is worth noting that the diagonal approximation yields an error near 1.0 at every timestep. This behavior indicates that the Fisher information matrix in diffusion models has most of its curvature concentrated in the off-diagonal terms, making the diagonal approximation particularly inadequate.

Our empirical results collectively suggest that the per-sample gradients are mostly collinear with their mean as SNR decreases and hence approximates a rank-1 structure that captures most of the curvatures in Fisher where a diagonal approximation fails.

3.3 EWC penalty with rank-1 Fisher

With the rank-1 approximation using Equation 5, we derive a practical EWC penalty term without forming a full Fisher matrix at each timestep and only use the gradients from the model. For simplicity of notation, let $g = g(\theta; x_t)$ and $\mu = \mu(\theta) = \mathbb{E}[g]$. From the empirical results in Figure 3a, the expectation averages both over data and timesteps. With $F(\theta) = \mathbb{E}\big[gg^\top\big]$, we have

$$\mu^\top F(\theta)\mu = \mu^\top \mathbb{E}\big[gg^\top\big]\mu = \mathbb{E}\big[(\mu^\top g)^2\big] \quad \Rightarrow \quad c^\star = \mathbb{E}[c_\theta^2(x_t)] = \frac{\mu^\top F(\theta)\mu}{\|\mu\|^4} = \frac{\mathbb{E}\big[(\mu^\top g)^2\big]}{\|\mu\|^4}.$$

Thus, plugging in $c^\star$ and Equation 5 into Equation 1, the EWC penalty with the rank-1 Fisher is:

$$\mathcal{L}_{\text{Rank-1}}(\theta) \;=\; \mathcal{L}_T(\theta) \;+\; \frac{\lambda}{2}\sum_{k=1}^{T-1} c_k^\star \left(\mu_k^\top(\theta - \theta_k^\star)\right)^2. \tag{6}$$

3.4 Promoting parameter sharing across tasks via generative distillation

EWC is most effective when the task optima lie in a shared parameter subspace, so that its quadratic penalty can steer gradient descent to a region that remains good for all tasks. In overparameterized models, however, different tasks can converge to disjoint basins, in which case no single parameter vector is simultaneously optimal, and the EWC penalty alone may fail.

To mitigate this limitation and strengthen our evaluation, we promote parameter sharing by adding a generative distillation term computed on replayed inputs from earlier tasks (Masip et al., 2025). Concretely, we keep a frozen teacher model $\varepsilon_{\theta^\star_{T-1}}$ from the previous task and sample replay inputs $\tilde{x}$ from it. Generative distillation then encourages the current model ε_θ to match the teacher model's denoising behavior:

$$\mathcal{L}_{\text{GD}}(\theta) \;=\; \mathbb{E}_{\tilde{x}\sim\tilde{\mathcal{D}}}\left[\frac{1}{2}\left\|\varepsilon_\theta(\tilde{x}) - \varepsilon_{\theta^\star_{T-1}}(\tilde{x})\right\|_2^2\right],$$

where $\tilde{\mathcal{D}}$ denotes the replay distribution. Our full objective becomes:

$$\mathcal{L}_{\text{total}}(\theta) = \mathcal{L}_{\text{Rank-1}}(\theta) + \mathcal{L}_{\text{GD}}(\theta) \tag{7}$$

Intuitively, the generative distillation term pulls ε_θ to remain compatible with past task behaviors on their input manifolds, guiding gradient descent toward regions that overlap with previous optima, thereby complementing EWC's curvature-based constraint.

4 Continual learning with rank-1 Fisher

As the Fisher of diffusion models is approximately rank-1, we validate the effectiveness of our findings on class-incremental continual learning tasks.

4.1 Datasets for class-incremental continual learning

In class-incremental continual learning, a dataset is partitioned into T tasks, where each task T_k contains n class labels and $\cap T_k = \emptyset$. We evaluate our approach on four image datasets commonly used in generative modeling: MNIST (Lecun et al., 1998), Fashion MNIST (FMNIST) (Xiao et al., 2017), CIFAR-10 (Krizhevsky, 2009), and ImageNet-1k (Deng et al., 2009). We use the down-sampled ImageNet-1k (Chrabaszcz et al., 2017) such that each image has the dimension of $3 \times 32 \times 32$ for faster training and evaluation while preserving similar performance characteristics to the full-size ImageNet-1k. We additionally pad MNIST and FMNIST to 32×32 to be consistent with CIFAR-10 and down-sampled ImageNet-1k. For each of MNIST, FMNIST, and CIFAR-10, we partition the dataset into 5 tasks with 2 classes per task. For ImageNet-1k, we partition it into 20 tasks with 50 classes per task, simulating a much longer horizon continual learning task. We use the same class label ordering as in the original dataset. We refer to Appendix D.3 for additional details.

4.2 Baselines and metrics

We compare our proposed EWC approach with a rank-1 Fisher approximation (Rank-1) against the widely used diagonal Fisher approximation (Diag), with both methods augmented by generative distillation as suggested in Section 3.4. For the ablation study, we compare both EWC approaches without generative distillation. In addition, we evaluate the generative distillation only (GD) approach to assess whether EWC provides complementary benefits beyond distillation. Finally, we compare these approaches to the non-continual learning setting, which serves as an upper bound for the performance. We hypothesize that with parameter sharing across tasks encouraged by generative distillation, a better Fisher approximation approach will lead to better continual learning performance and will complement generative distillation.

Metrics. To evaluate continual learning performance for generative models, we compute the Fréchet Inception Distance (FID; Heusel et al., 2018) between generated samples and each task's held-out test set. Let m_k be the model after training on tasks $1{:}k$, and let $\mathrm{FID}_i(m_k)$ denote the FID on task i's test set when evaluated with m_k. We report two primary metrics:

- **Average FID through task k.** $\mathcal{A}\mathrm{FID}@k = \frac{1}{k}\sum_{i=1}^{k}\mathrm{FID}_i(m_k)$, so $\mathcal{A}\mathrm{FID}@T$ summarizes overall performance at the end of training.
- **Final average forgetting.** $\mathcal{F} = \frac{1}{T}\sum_{k=1}^{T}\Big(\mathrm{FID}_k(m_T) - \mathrm{FID}_k(m_k)\Big)$, the mean change in each task's FID immediately after it is learned (m_k) as compared to after training on all tasks (m_T).

4.3 Implementation details

We use the label conditioning UNet implementation from *Huggingface* with default hyper-parameters as our denoising network. We use 4 ResNet blocks with 128 output channels in the first down-sample block and 256 output channels in the rest. For sampling, we use a DDIM scheduler with 50 sampling steps and 1000 noising steps. We train our UNet with 100 epochs on ImageNet-1k and 200 epochs on the rest of the datasets for each task with a batch size of 128 and a learning rate of 2×10^{-4} using Adam (Kingma & Ba, 2017). We use an EWC penalty weight of 15000 for all tasks. For generative distillation, we create a replay buffer of 1300 images per class for ImageNet-1k and 5000 images per class for other datasets. We refer to Appendix C for additional training details.

5 Results and Discussions

5.1 Continual learning performance

EWC complements generative distillation. We report the average FID at the final task as a comprehensive measure of performance and forgetting for each dataset and method in Table 1. Our results show that without generative distillation, EWC alone struggles to maintain a shared optimum across tasks, leading to degraded continual learning performance on all datasets. The consistently high forgetting indicates that the EWC penalty pulls the model toward the previous task's optimum while moving it away from the current task's, suggesting little to no overlap between task optima.

Using generative distillation alone substantially improves both average FID and forgetting on all datasets compared to EWC-only by encouraging the model to move toward an optima that performs well across all (including replayed) tasks. When combined with our rank-1 EWC, we observe further improvements on all datasets. On MNIST and FMNIST, catastrophic forgetting is nearly eliminated

Table 1: Average FID at the final task and average forgetting across methods and datasets. Standard errors are reported over 3 random seeds.

Methods	**MNIST**		**FMNIST**		**CIFAR-10**		**ImageNet-1k**	
	$\mathcal{A}$FID↓	$\mathcal{F}$↓	$\mathcal{A}$FID↓	$\mathcal{F}$↓	$\mathcal{A}$FID↓	$\mathcal{F}$↓	$\mathcal{A}$FID↓	$\mathcal{F}$↓
Non-continual	$2.6_{\pm 0.1}$	–	$5.7_{\pm 0.8}$	–	$23.3_{\pm 0.7}$	–	$11.7_{\pm 0.1}$	–
Diag$_{\text{w/o GD}}$	$62.2_{\pm 2.9}$	$51.1_{\pm 4.2}$	$99.9_{\pm 3.5}$	$81.7_{\pm 4.7}$	$128.6_{\pm 4.6}$	$74.4_{\pm 3.5}$	$86.1_{\pm 4.2}$	$34.2_{\pm 3.6}$
Rank-1$_{\text{w/o GD}}$	$65.2_{\pm 4.6}$	$58.3_{\pm 4.4}$	$96.9_{\pm 3.2}$	$82.1_{\pm 3.5}$	$120.0_{\pm 10.2}$	$77.4_{\pm 9.4}$	$74.3_{\pm 1.9}$	$41.3_{\pm 1.8}$
GD	$10.1_{\pm 0.9}$	$2.3_{\pm 0.8}$	$19.1_{\pm 0.9}$	$3.9_{\pm 0.5}$	$61.2_{\pm 3.2}$	$16.6_{\pm 0.6}$	$69.0_{\pm 2.2}$	$46.2_{\pm 12.9}$
Diag	$14.3_{\pm 1.3}$	$5.2_{\pm 1.2}$	$27.7_{\pm 2.2}$	$9.1_{\pm 2.7}$	$72.6_{\pm 3.2}$	$17.9_{\pm 1.8}$	$73.8_{\pm 2.8}$	$25.8_{\pm 9.4}$
Rank-1 (ours)	$\mathbf{7.6}_{\pm 0.1}$	$\mathbf{0.6}_{\pm 0.1}$	$\mathbf{15.4}_{\pm 0.6}$	$\mathbf{0.9}_{\pm 0.3}$	$\mathbf{50.5}_{\pm 1.2}$	$\mathbf{7.4}_{\pm 1.2}$	$\mathbf{48.5}_{\pm 1.9}$	$\mathbf{15.2}_{\pm 4.8}$

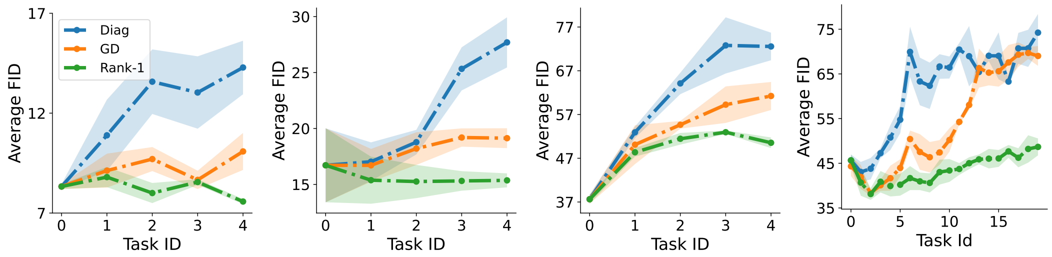

(a) MNIST (b) FMNIST (c) CIFAR-10 (d) ImageNet-1k

Figure 4: Average FID at each task during continual learning on evaluated datasets. Standard errors are averaged over 3 random seeds.

with forgetting $\mathcal{F} = 0.6_{\pm 0.1}$ and $\mathcal{F} = 0.9_{\pm 0.3}$, respectively. On the long horizon ImageNet-1k dataset, rank-1 EWC halves forgetting relative to generative distillation alone ($\mathcal{F} = 15.2_{\pm 0.1}$ vs. $\mathcal{F} = 31.6_{\pm 0.2}$). And across all datasets, image generation quality improves substantially, further narrowing the gap to the non-continual upper bound. In contrast, while combining diagonal EWC with distillation improves the diagonal EWC-only approach, the improvement stems largely from distillation, and performance often matches or even degrades compared to distillation alone, suggesting the ineffectiveness of the diagonal EWC constraint. Overall, these results demonstrate that rank-1 EWC effectively complements generative distillation by enforcing parameter constraints within the shared optimum that distillation provides.

Rank-1 EWC is stable and robust on long horizon tasks. To study the learning dynamics during continual learning on evaluated datasets, we plot the average FID at each task in Figure 4. Our results show that rank-1 EWC with distillation consistently reaches a lower average FID during learning on all datasets than distillation-only and the diagonal variant. Surprisingly, on MNIST and FMNIST, average FID even decreases as the model learns new tasks. Given the near-zero positive forgetting from Table 1, Figure 4 suggests that the generation quality on some tasks improve when learning new tasks. This improvement in generation quality on early trained tasks can also be found in CIFAR-10 where the average FID decreases at the final task. This finding implies that our rank-1 EWC approach not only effectively constrained the model updates to preserve knowledge on the old tasks, but also refining old knowledge based on new tasks.

In addition, on the long horizon ImageNet-1k dataset, both generative distillation-only and the diagonal variant begin to diverge around task 10 while the average FID only gradually increases for our rank-1 approach. In particular, the generative distillation-only approach reached a plateau around task 6 to 11 before diverging. This suggests that distillation suffers from distribution shift due to errors that have accumulated from the previous imperfect replay samples, such that the model optima moves away from early tasks. We refer Appendix D.4 for additional results.

5.2 Qualitative analysis

To visually inspect how image generation quality evolves during continual learning, we fix a label class and, after each task, sample images from that class and plot them in sequence. Figure 5 illustrates

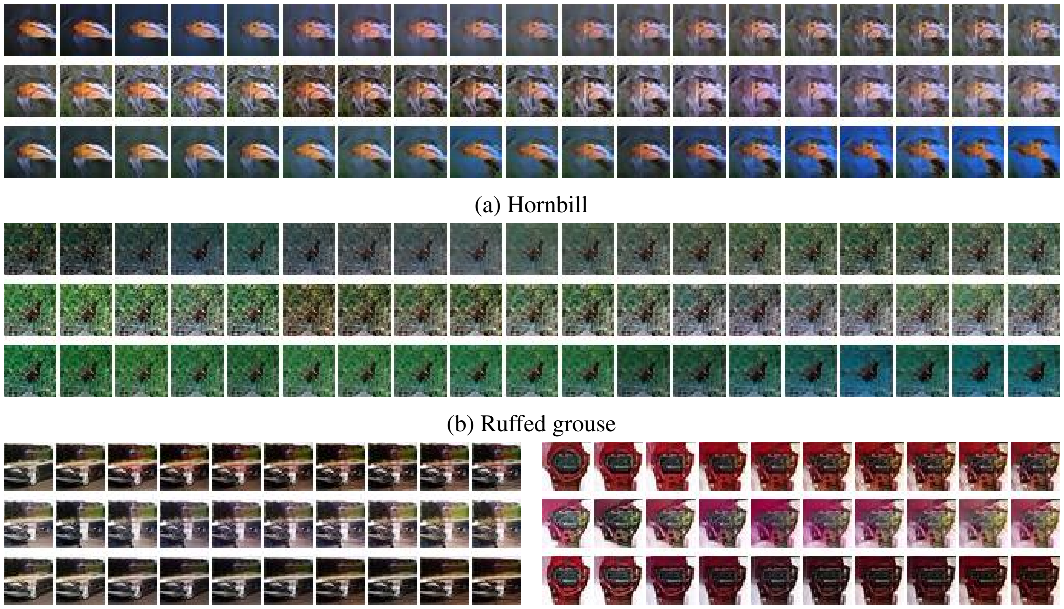

(a) Hornbill

(b) Ruffed grouse

(c) Convertible

(d) Digital Watch

Figure 5: Examples of generated images from selected classes in ImageNet-1k over continual learning tasks. (a) Hornbill class sampled from models trained on task 1 to 19. (b) Ruffed grouse class from task 1 to 19. (c) Convertible class from task 10 to 19. (d) Digital watch class from task 10 to 19. Top row: generative distillation-only; middle row: diagonal; bottom row: rank-1.

ImageNet-1k examples: the hornbill and the ruffed grouse classes sampled from models trained on task 1-19 (Figs. 5a and 5b), the convertible and the digital watch classes sampled from models trained on tasks 10–19 (Figs. 5c and 5d). Our results show that both generative distillation-only (top row) and the diagonal variant (middle row) progressively generate a noisier sample as continual learning progresses to later tasks. On the other hand, rank-1 EWC with generative distillation maintains the sharpness of the objects. For example, both ruffed grouse and digital watch remain intact while other approaches almost distort the central object in the later tasks. Our results show that the proposed rank-1 method consistently preserves image quality across tasks, whereas images generated by the diagonal variant and generative distillation-only progressively become noisy and less recognizable.

6 Conclusion, limitations, and future work

In this paper, we investigate gradients in diffusion models and show that per-sample gradients become approximately collinear with their population mean when the SNR is low, inducing an effective rank-1 Fisher information matrix. Leveraging this structure, we hypothesized and validated that a rank-1 Fisher provides a better approximation for EWC than the commonly used diagonal Fisher approximation. When paired with generative distillation, which encourages cross-task parameter sharing that EWC assumes, our method improves continual learning performance. On class-incremental image generation, rank-1 EWC with generative distillation outperforms both generative distillation-only and diagonal Fisher EWC across MNIST, FMNIST, CIFAR-10, and ImageNet-1k in terms of lower average FID and reduced forgetting. In particular, forgetting is nearly eliminated on MNIST and FMNIST and is roughly halved on ImageNet-1k, the longest-horizon setting, relative to generative distillation-only. These findings indicate that diffusion models admit an effective rank-1 Fisher; with this better Fisher approximation, EWC complements replay by constraining replay-induced distribution drift toward a shared parameter region that supports all tasks.

Limitations and future work. Assumption 1 suggests that the collinearity of per-sample gradients is dependent on the denoising network's architecture. While current work focuses on the UNet-based diffusion models, as this is a popular architecture, future work should expand our analysis to more recent architectures, such as those used in Transformer-based diffusion models (Peebles & Xie, 2023).

REPRODUCIBILITY STATEMENT

We used open-source datasets and model implementations as described in Section 3.2 and Section 4, and additional experiment details, including empirical validation experiment implementations, class-incremental dataset splits, and hyper-parameters in Appendices C and D.3.

REFERENCES

Jingfan Chen, Yuxi Wang, Pengfei Wang, Xiao Chen, Zhaoxiang Zhang, Zhen Lei, and Qing Li. DiffusePast: Diffusion-based generative replay for class incremental semantic segmentation. *arXiv preprint arXiv:2308.01127*, 2023.

Patryk Chrabaszcz, Ilya Loshchilov, and Frank Hutter. A downsampled variant of imagenet as an alternative to the cifar datasets, 2017. URL `https://arxiv.org/abs/1707.08819`.

Jia Deng, Wei Dong, Richard Socher, Li-Jia Li, Kai Li, and Li Fei-Fei. Imagenet: A large-scale hierarchical image database. In *2009 IEEE Conference on Computer Vision and Pattern Recognition*, pp. 248–255, 2009. doi: 10.1109/CVPR.2009.5206848.

Bradley Efron. Tweedie's formula and selection bias. *Journal of the American Statistical Association*, 106(496):1602–1614, 2011.

David J Foster and Matthew A Wilson. Reverse replay of behavioural sequences in hippocampal place cells. *Nature*, 440(7084):680–683, 2006.

Robert M French. Catastrophic forgetting in connectionist networks. *Trends in Cognitive Sciences*, 3 (4):128–135, 1999.

Ruikang Gao et al. DDGR: Continual learning with deep diffusion-based generative replay. In *Proceedings of the 40th International Conference on Machine Learning*, volume 202 of *Proceedings of Machine Learning Research*, 2023. URL `https://proceedings.mlr.press/v202/gao23e.html`.

Martin Heusel, Hubert Ramsauer, Thomas Unterthiner, Bernhard Nessler, and Sepp Hochreiter. Gans trained by a two time-scale update rule converge to a local nash equilibrium, 2018. URL `https://arxiv.org/abs/1706.08500`.

Jonathan Ho, Ajay Jain, and Pieter Abbeel. Denoising diffusion probabilistic models. In *Advances in Neural Information Processing Systems*, 2020a. arXiv:2006.11239.

Jonathan Ho, Ajay Jain, and Pieter Abbeel. Denoising diffusion probabilistic models. In *NeurIPS*, 2020b.

Aapo Hyvärinen. Estimation of non-normalized statistical models by score matching. *Journal of Machine Learning Research*, 6:695–709, 2005.

Junsu Kim, Hoseong Cho, Jihyeon Kim, Yihalem Y. Tiruneh, and Seungryul Baek. SDDGR: Stable diffusion-based deep generative replay for class incremental object detection. In *Proceedings of the IEEE/CVF Conference on Computer Vision and Pattern Recognition*, 2024. URL `https://openaccess.thecvf.com/content/CVPR2024/papers/Kim_SDDGR_Stable_Diffusion-based_Deep_Generative_Replay_for_Class_Incremental_Object_CVPR_2024_paper.pdf`.

Diederik P. Kingma and Jimmy Ba. Adam: A method for stochastic optimization, 2017. URL `https://arxiv.org/abs/1412.6980`.

James Kirkpatrick, Razvan Pascanu, Neil Rabinowitz, Joel Veness, Guillaume Desjardins, Andrei A. Rusu, Kieran Milan, John Quan, Tiago Ramalho, Agnieszka Grabska-Barwinska, Demis Hassabis, Claudia Clopath, Dharshan Kumaran, and Raia Hadsell. Overcoming catastrophic forgetting in neural networks. *Proceedings of the National Academy of Sciences*, 114(13):3521–3526, March 2017. ISSN 1091-6490. doi: 10.1073/pnas.1611835114. URL `http://dx.doi.org/10.1073/pnas.1611835114`.

Alex Krizhevsky. Learning multiple layers of features from tiny images. Technical report, University of Toronto, 2009.

Y. Lecun, L. Bottou, Y. Bengio, and P. Haffner. Gradient-based learning applied to document recognition. *Proceedings of the IEEE*, 86(11):2278–2324, 1998. doi: 10.1109/5.726791.

Sergio Masip et al. Continual learning of diffusion models with generative distillation. In *Proceedings of Machine Learning Research*, 2025. URL `https://proceedings.mlr.press/v274/masip25a.html`.

James L McClelland, Bruce L McNaughton, and Randall C O'Reilly. Why there are complementary learning systems in the hippocampus and neocortex: insights from the successes and failures of connectionist models. *Psychological Review*, 102(3):419–457, 1995.

Michael McCloskey and Neal J Cohen. Catastrophic interference in connectionist networks: The sequential learning problem. *Psychology of Learning and Motivation*, 24:109–165, 1989.

James L McGaugh. Memory–a century of consolidation. *Science*, 287(5451):248–251, 2000.

Alex Nichol and Prafulla Dhariwal. Improved denoising diffusion probabilistic models. In *ICML*, 2021.

German I Parisi et al. Continual lifelong learning with neural networks: A review. *Neural Networks*, 113:54–71, 2019.

William Peebles and Saining Xie. Scalable diffusion models with transformers, 2023. URL `https://arxiv.org/abs/2212.09748`.

Olaf Ronneberger, Philipp Fischer, and Thomas Brox. U-net: Convolutional networks for biomedical image segmentation, 2015. URL `https://arxiv.org/abs/1505.04597`.

Jonathan Schwarz et al. Progress & compress: A scalable framework for continual learning. In *ICML*, pp. 4528–4537, 2018.

Hanul Shin, Jung Kwon Lee, Jaehong Kim, and Jiwon Kim. Continual learning with deep generative replay. In *NeurIPS*, 2017.

Jascha Sohl-Dickstein, Eric A. Weiss, Niru Maheswaranathan, and Surya Ganguli. Deep unsupervised learning using nonequilibrium thermodynamics. In *International Conference on Machine Learning*, pp. 2256–2265, 2015.

Jiaming Song, Chenlin Meng, and Stefano Ermon. Denoising diffusion implicit models. In *International Conference on Learning Representations*, 2021a. arXiv:2010.02502.

Yang Song and Stefano Ermon. Generative modeling by estimating gradients of the data distribution. In *Advances in Neural Information Processing Systems*, 2019.

Yang Song, Jascha Sohl-Dickstein, Diederik P. Kingma, Abhishek Kumar, Stefano Ermon, and Ben Poole. Score-based generative modeling through stochastic differential equations. *International Conference on Learning Representations*, 2021b. openreview.net/forum?id=PxTIG12RRHS.

Gido M van de Ven and Andreas S Tolias. Generative replay with feedback connections as a general strategy for continual learning. In *NeurIPS*, 2018.

Pascal Vincent. A connection between score matching and denoising autoencoders. *Neural Computation*, 23(7):1661–1674, 2011. doi: 10.1162/NECO_a_00142.

Han Xiao, Kashif Rasul, and Roland Vollgraf. Fashion-mnist: a novel image dataset for benchmarking machine learning algorithms, 2017. URL `https://arxiv.org/abs/1708.07747`.

A THE USE OF LARGE LANGUAGE MODELS

We primarily use LLMs to improve wording and sentence structure, check grammar, and reorganize or document code.

B Additional proofs

B.1 Proof for proposition 1

Proof. By Tweedie's identity, write $s_t^\star(x_t) = \frac{\sqrt{\bar{\alpha}_t}}{1-\bar{\alpha}_t}\mathbb{E}[x_0 \mid x_t] - x_t/(1-\bar{\alpha}_t)$. As $\bar{\alpha}_t$ decreases with timestep due to DDPM's linear noise scheduler, SNR= $\frac{\sqrt{\bar{\alpha}_t}}{1-\bar{\alpha}_t}$ decreases with t. And because $\frac{\sqrt{\bar{\alpha}_t}}{1-\bar{\alpha}_t}$ decreases faster than $1/(1-\bar{\alpha}_t)$, $s_t^\star(x_t) \approx -x_t/(1-\bar{\alpha}_t)$. □

B.2 Proof for proposition 2

Proof. Let $g(\theta; x_t) = \nabla_\theta \mathcal{L}_{\text{DSM}}(\theta; x_t)$, $\mu(\theta) = \mathbb{E}_{x_t' \sim q_t}\big[g(\theta; x_t')\big]$. By Proposition 1, $s^\star(x_t) \approx x_t\gamma_t$, where $\gamma_t = -1/(1-\bar{\alpha}_t)$ is a scalar independent of x_t. Near convergence, the denoising network approximates the true score function: $s_\theta(x_t, t) \approx s^\star(x_t) \approx x_t\gamma_t$. By Assumption 1, $s_\theta(x_t, t)$ takes a linear form as $s_\theta(x_t, t) = x_t\theta$. Substitute back to $g(\theta; x_t)$:

$$g(\theta; x_t) = \nabla_\theta \left(\frac{1-\bar{\alpha}_t}{2}\big\|s_\theta(x_t, t) - s^\star(x_t)\big\|_2^2\right) \tag{8}$$

$$= \nabla_\theta \left(\frac{1-\bar{\alpha}_t}{2}\big\|x_t\theta - x_t\gamma_t\big\|_2^2\right) \tag{9}$$

$$= (1-\bar{\alpha}_t)\big(x_t\theta - x_t\gamma_t I\big)x_t^\top \tag{10}$$

$$= (1-\bar{\alpha}_t)\|x_t\|^2(\theta - \gamma_t I). \tag{11}$$

Let $c(x_t) = (1-\bar{\alpha}_t)\|x_t\|^2$ be a scalar function dependent on x_t, and $v = \theta - \gamma_t I$ be a vector in parameter space doesn't depend on x_t. Then $g(\theta; x_t) = c(x_t)v$. By the definition of collinearity, $g(\theta; x_t)$ collinear with v for any $x_t \sim q_t$. And since per-sample gradient collinear with each other, it collinear with the population mean $\mu(\theta)$. □

C Empirical Results

This section provides implementation details for the empirical study presented in the main text.

We use the label-conditioned `UNet` implementation from *HuggingFace* as the denoising backbone. The base model consists of three ResNet blocks per downsampling stage, each with 16 output channels and two layers per block.

Training is performed with a batch size of 128 and learning rate 2×10^{-4} using the Adam optimizer (Kingma & Ba, 2017). Each task is trained for 200 epochs on the full dataset. On MNIST (Lecun et al., 1998), training the base model required approximately 97 minutes on a single Nvidia A100 (40GB) GPU.

C.1 Additional Model Variants

To assess whether the observed Fisher structure depends on model capacity, we trained two reduced variants of the UNet under identical hyperparameters:

1. **Small-1:** one ResNet block with 16 output channels and a single layer per block;
2. **Small-3:** three ResNet blocks with 16 output channels each, but only one layer per block.

Both models were trained for 200 epochs per task with batch size 128 and learning rate 2×10^{-4}. On MNIST, training required $\sim$ 56 minutes for Small-1 and $\sim$ 78 minutes for Small-3, compared to 97 minutes for the base model.

While all variants display the same qualitative trends—eigenspectrum decay (Figs. 6a and 6c) and dominance of a single eigenvalue (Figs. 6b and 6d)—we observe that the empirical rank-1 behavior becomes more pronounced as model size increases. This suggests that our theoretical predictions are not artifacts of small networks, but rather strengthen with scale. Theoretically, this follows from our optimality assumption: larger models are expected to achieve solutions closer to the optimal point, thereby aligning more closely with the conditions under which the Fisher reduces to a rank-1 structure. Consequently, one should expect the rank-1 Fisher approximation to hold even more robustly in larger, real-world diffusion models.

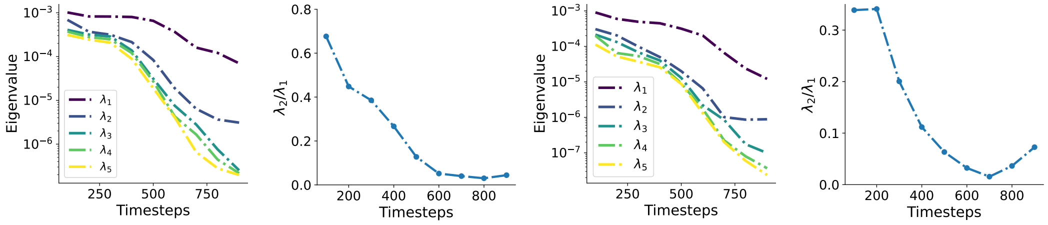

(a) (b) (c) (d)

Figure 6: Eigenvalue analysis of the empirical Fisher for reduced UNet variants. Panels (a) and (b) show the top 5 eigenvalues (log-scale) and eigengap ratios $r_t = \lambda_2/\lambda_1$ across timesteps for the **Small-1** model, while panels (c) and (d) report the same quantities for the **Small-3** model. In both cases, the Fisher remains nearly rank-1, with the leading eigenvalue λ_1 dominating and the eigengap widening as model size increases.

D Continual Learning Results

D.1 Additional Implementation Details

We use the label-conditioned UNet implementation from *Huggingface* as our denoising network. The UNet employs three ResNet blocks with 16 output channels in each downsampling block. For training, we use a batch size of 128 and a learning rate of 2×10^{-4} with the Adam optimizer (Kingma & Ba, 2017), and train for 200 epochs per task for each dataset.

Training was performed on a single Nvidia A100 40GB GPU, taking a total of 157 minutes.

D.2 Additional implementation details for continual learning experiments

We employ a label-conditioned UNet implementation from *HuggingFace* as our denoising network, retaining the default hyper-parameters. The architecture consists of four ResNet blocks, with 128 output channels in the first down-sampling block and 256 output channels in the remaining blocks. For sampling, we use a DDIM scheduler with 50 sampling steps and 1000 noising steps.

We summarize our training hyperparameters in Table 2. Unless otherwise stated, the same settings are used across all datasets and tasks. We also provide the average runtime (including FID evaluation) for each dataset and method in Table 3.

Table 2: Training configurations used across datasets.

Setting	**Value**
Optimizer	Adam (Kingma & Ba, 2017)
Learning Rate	2×10^{-4}
Batch Size	128
Training Epochs	200 per task
EWC Penalty Weight	15000
Replay Buffer (ImageNet-1k)	1300 images per class
Replay Buffer (others)	5000 images per class

D.3 Additional Dataset Details

All datasets are resized or padded to 32×32 for consistency. Table 4 summarizes their configurations.

Table 3: Average training runtime (hours) and GPU used per dataset/method.

Dataset	Method	Hours	GPU
MNIST	Diag	~ 5	NVIDIA L40S
MNIST	Rank-1	~ 5	NVIDIA L40S
MNIST	GR	~ 8	NVIDIA L40S
MNIST	Diag + GR	~ 9	NVIDIA L40S
MNIST	Rank-1 + GR	~ 9	NVIDIA L40S
FMNIST	Diag	~ 5	NVIDIA L40S
FMNIST	Rank-1	~ 5	NVIDIA L40S
FMNIST	GR	~ 8	NVIDIA L40S
FMNIST	Diag + GR	~ 9	NVIDIA L40S
FMNIST	Rank-1 + GR	~ 9	NVIDIA L40S
CIFAR-10	Diag	~ 4	NVIDIA L40S
CIFAR-10	Rank-1	~ 4	NVIDIA L40S
CIFAR-10	GR	~ 7	NVIDIA L40S
CIFAR-10	Diag + GR	~ 8	NVIDIA L40S
CIFAR-10	Rank-1 + GR	~ 8	NVIDIA L40S
ImageNet-1k	Diag	~ 25	NVIDIA H200
ImageNet-1k	Rank-1	~ 24	NVIDIA H200
ImageNet-1k	GR	~ 64	NVIDIA H200
ImageNet-1k	Diag + GR	~ 71	NVIDIA H200
ImageNet-1k	Rank-1 + GR	~ 70	NVIDIA H200

Dataset	#Training Images per Task	#Tasks	Description of Each Task
MNIST (Lecun et al., 1998)	12,000	5	Generation of 2 classes of handwritten digits
Fashion-MNIST (Xiao et al., 2017)	12,000	5	Generation of 2 classes of fashion products
CIFAR-10 (Krizhevsky, 2009)	10,000	5	Generation of 2 classes of common items
ImageNet-1k (Chrabaszcz et al., 2017)	~64,000	20	Generation of 50 classes of ImageNet objects

Table 4: Detailed dataset configurations and task partitions used in our experiments.

MNIST. A dataset of handwritten digits (0–9) with 60,000 training and 10,000 test images. Each task contains two digit classes.
Task splits: $T_1 = \{0, 1\},\ T_2 = \{2, 3\},\ T_3 = \{4, 5\},\ T_4 = \{6, 7\},\ T_5 = \{8, 9\}$.

Fashion MNIST.
A dataset of 10 grayscale clothing categories (e.g., shirts, shoes, bags) with 60,000 training and 10,000 test images. Each task contains two categories.
Task splits: $T_1 = \{0, 1\},\ T_2 = \{2, 3\},\ T_3 = \{4, 5\},\ T_4 = \{6, 7\},\ T_5 = \{8, 9\}$.

CIFAR-10.
A dataset of 32 × 32 RGB images across 10 classes (e.g., animals, vehicles) with 50,000 training and 10,000 test images. Each task contains two classes.
Task splits: $T_1 = \{0, 1\},\ T_2 = \{2, 3\},\ T_3 = \{4, 5\},\ T_4 = \{6, 7\},\ T_5 = \{8, 9\}$.

ImageNet-1k (downsampled).
A large-scale dataset with 1,000 object categories and 1.28 million training images. We use the 32 × 32 downsampled version for computational efficiency. Each task contains fifty classes.
Task splits: $T_1 = \{0, \ldots, 49\},\ T_2 = \{50, \ldots, 99\},\ \ldots\ T_{20} = \{950, \ldots, 999\}$.

D.4 Continual Learning Curves for each Task and Dataset

We provide a comprehensive set of FID evaluation plots for all tasks across the datasets considered in our experiments. These plots illustrate the model's performance on individual tasks and complement the quantitative results presented in the main paper.

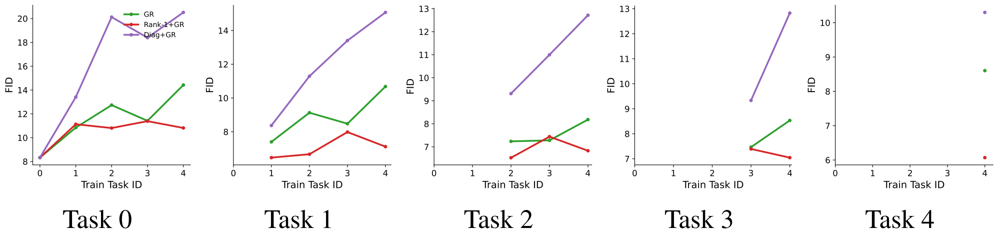

Task 0 Task 1 Task 2 Task 3 Task 4

Figure 7: FID plots for MNIST (generative replay).

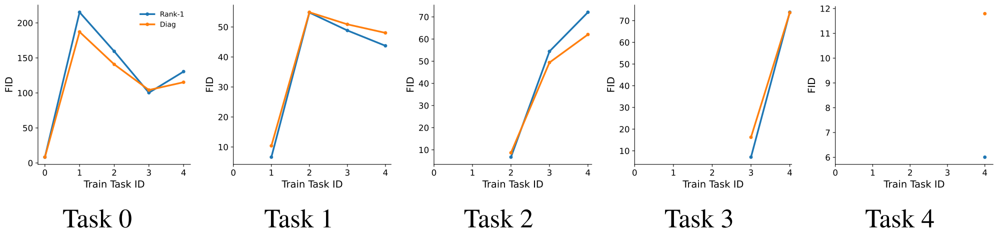

Task 0 Task 1 Task 2 Task 3 Task 4

Figure 8: FID plots for MNIST (non-generative replay).

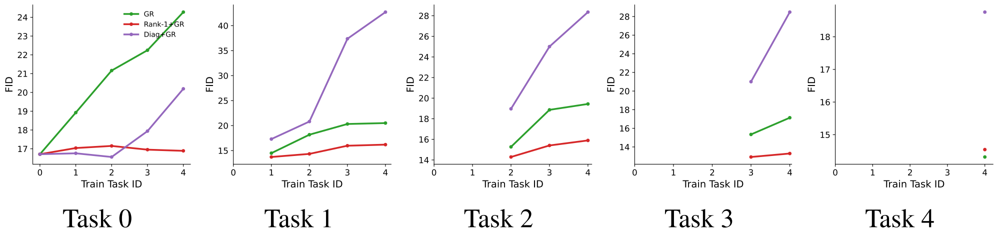

Task 0 Task 1 Task 2 Task 3 Task 4

Figure 9: FID plots for Fashion-MNIST (generative replay).

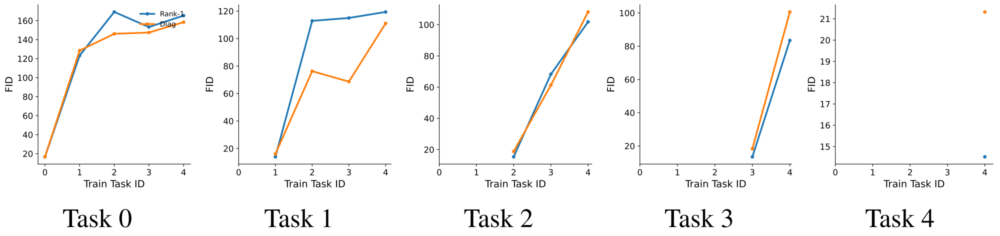

Task 0 Task 1 Task 2 Task 3 Task 4

Figure 10: FID plots for Fashion-MNIST (non-generative replay).

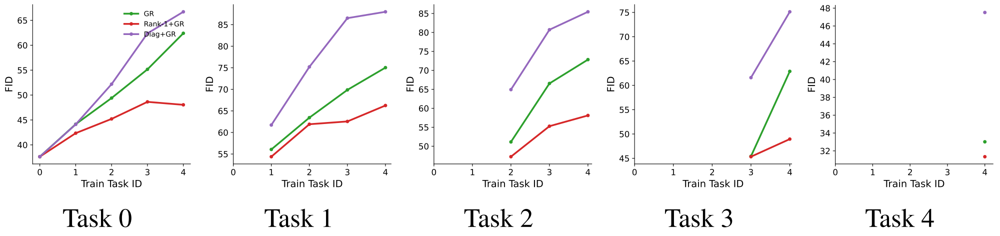

Task 0 Task 1 Task 2 Task 3 Task 4

Figure 11: FID plots for CIFAR-10 (generative replay).

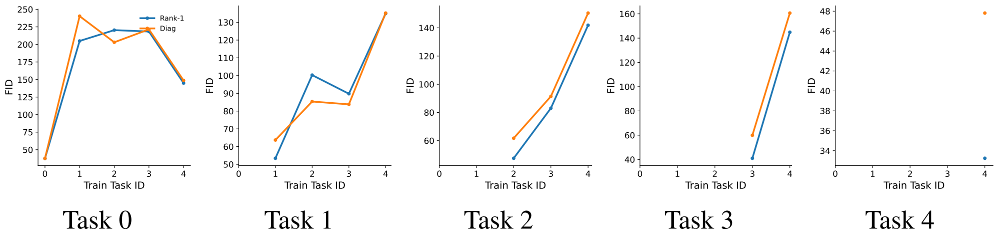

Task 0 Task 1 Task 2 Task 3 Task 4

Figure 12: FID plots for CIFAR-10 (non-generative replay).

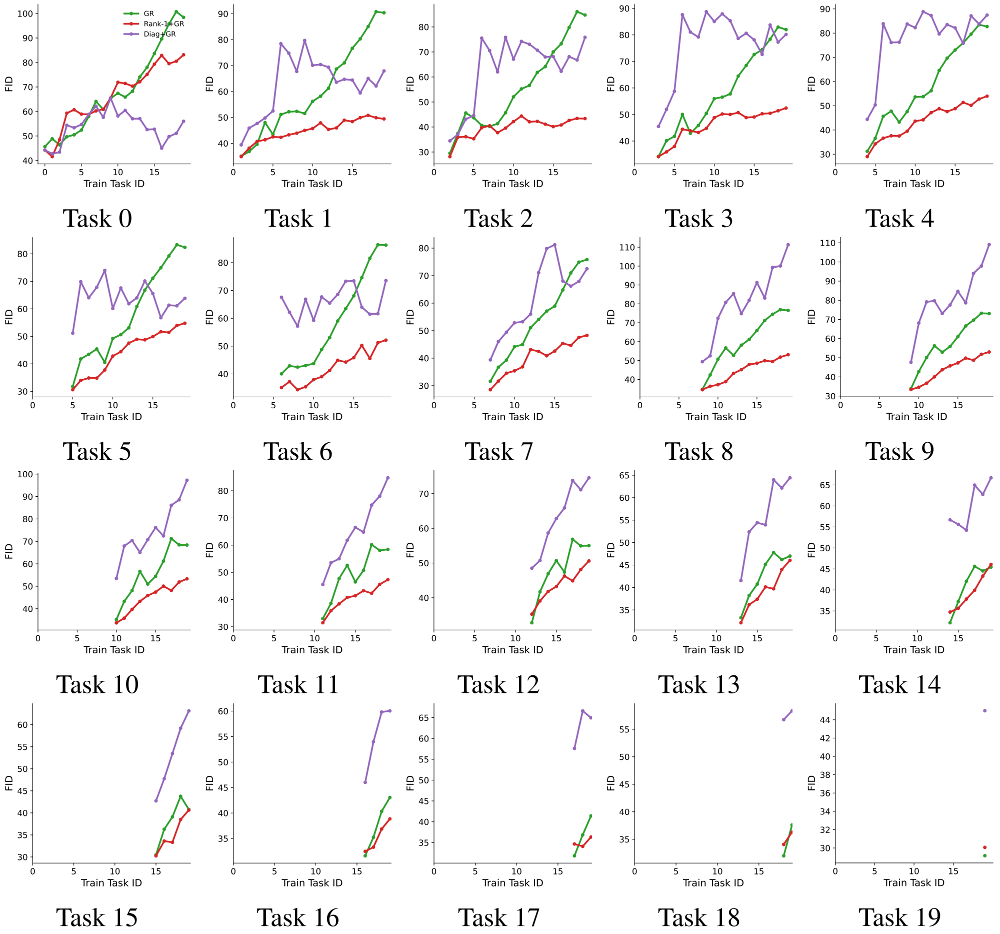

Task 0 Task 1 Task 2 Task 3 Task 4

Task 5 Task 6 Task 7 Task 8 Task 9

Task 10 Task 11 Task 12 Task 13 Task 14

Task 15 Task 16 Task 17 Task 18 Task 19

Figure 13: FID plots for Imagenet-1k (generative replay).

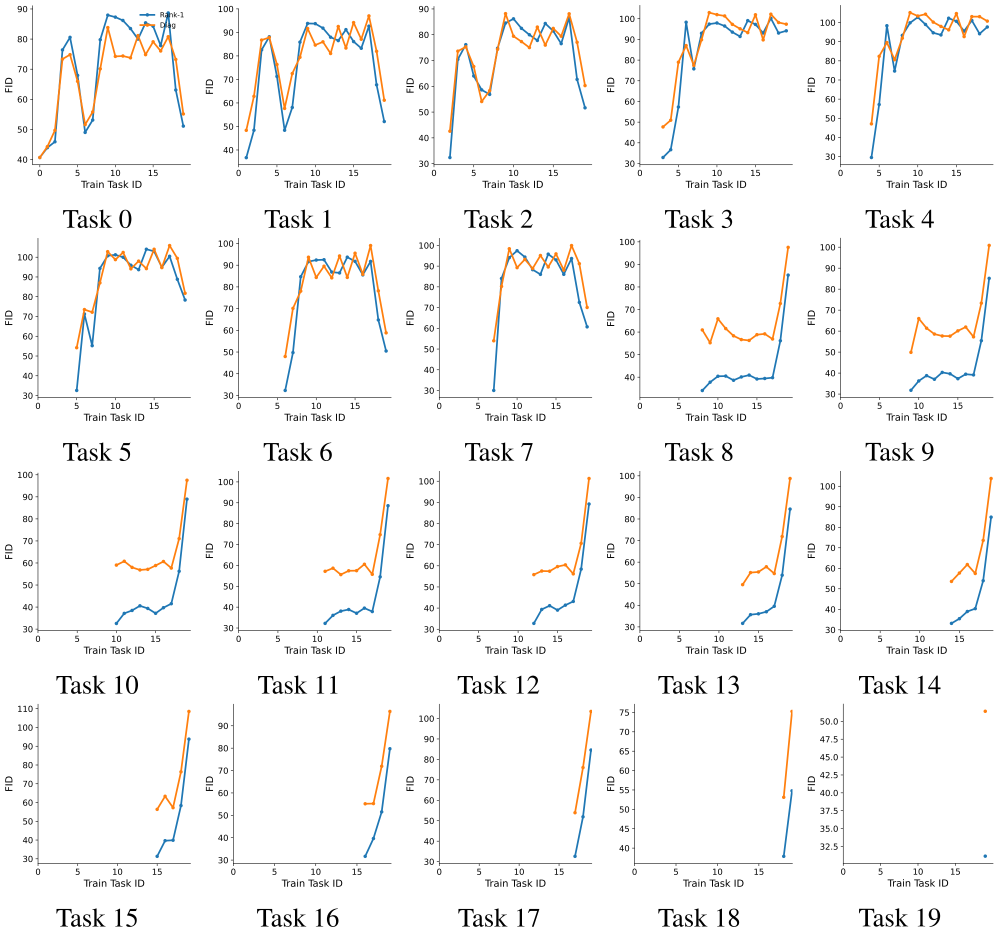

Task 0 Task 1 Task 2 Task 3 Task 4

Task 5 Task 6 Task 7 Task 8 Task 9

Task 10 Task 11 Task 12 Task 13 Task 14

Task 15 Task 16 Task 17 Task 18 Task 19

Figure 14: FID plots for Imagenet-1k (non-generative replay).